

Electrical transport and optical properties of Cd_3As_2 thin films

Yun-Kun Yang(杨运坤), Fa-Xian Xiu(修发贤), Feng-Qiu Wang(王枫秋), Jun Wang(王军), Yi Shi(施毅)
Citation: Chin. Phys. B . 2019, 28(10): 107502 . **doi:** 10.1088/1674-1056/28/10/107502
Journal homepage: http://cpb.iphy.ac.cn; http://iopscience.iop.org/cpb

What follows is a list of articles you may be interested in

Thickness dependent manipulation of uniaxial magnetic anisotropy in Fe-thin films by oblique deposition

Qeemat Gul, Wei He(何为), Yan Li(李岩), Rui Sun(孙瑞), Na Li(李娜), Xu Yang(杨旭), Yang Li(李阳), Zi-Zhao Gong(弓子召), ZongKai Xie(谢宗凯), Xiang-Qun Zhang(张向群), Zhao-Hua Cheng(成昭华)
Chin. Phys. B . 2018, 27(9): 097504 . **doi:** 10.1088/1674-1056/27/9/097504

Low temperature ferromagnetic properties of CdS and CdTe thin films

Hafiz Tariq Masood, Zahir Muhammad, Muhammad Habib, Dong-Ming Wang(王东明), De-Liang Wang(王德亮)
Chin. Phys. B . 2017, 26(6): 067503 . **doi:** 10.1088/1674-1056/26/6/067503

High frequency magnetic properties of ferromagnetic thin films and magnetization dynamics of coherent precession

Jiang Chang-Jun, Fan Xiao-Long, Xue De-Sheng
Chin. Phys. B . 2015, 24(5): 057504 . **doi:** 10.1088/1674-1056/24/5/057504

Magnetic behaviors of cerium oxide-based thin films deposited using electrochemical method

Peng Ying-Zi, Li Yuan, Bai Ru, Huo De-Xuan, Qian Zheng-Hong
Chin. Phys. B . 2014, 23(9): 097503 . **doi:** 10.1088/1674-1056/23/9/097503

Flexible tuning microwave permeability spectrum in $[ferromagnet/antiferromagnet]_n$ exchange-biasedmultilayer stack structure

Jin Li-Chuan, Zhang Huai-Wu, Tang Xiao-Li, Bai Fei-Ming, Zhong Zhi-Yong
Chin. Phys. B . 2013, 22(4): 047502 . **doi:** 10.1088/1674-1056/22/4/047502

TOPICAL REVIEW — A celebration of the 100th birthday of Kun Huang

Electrical transport and optical properties of Cd_3As_2 thin films*

Yun-Kun Yang(杨运坤)[1,2], Fa-Xian Xiu(修发贤)[1,2], Feng-Qiu Wang(王枫秋)[1,3], Jun Wang(王军)[4,5], and Yi Shi(施毅)[1,3,6,†]

[1] *Collaborative Innovation Center of Advanced Microstructures, Nanjing* 210093, *China*
[2] *State Key Laboratory of Surface Physics and Department of Physics, Fudan University, Shanghai* 200433, *China*
[3] *School of Electronic Science and Engineering, Nanjing University, Nanjing* 210093, *China*
[4] *School of Optoelectronic Science and Engineering, University of Electronic Science and Technology of China, Chengdu* 610054, *China*
[5] *State Key Laboratory of Electronic Thin Films and Integrated Devices, University of Electronic Science and Technology of China, Chengdu* 610054, *China*
[6] *National Laboratory of Solid State Microstructures, School of Physics, Nanjing University, Nanjing* 210093, *China*

(Received 17 July 2019; revised manuscript received 8 August 2019; published online 28 August 2019)

Cd_3As_2, as a three-dimensional (3D) topological Dirac semimetal, has attracted wide attention due to its unique physical properties originating from the 3D massless Dirac fermions. While many efforts have been devoted to the exploration of novel physical phenomena such as chiral anomaly and phase transitions by using bulk crystals, the development of high-quality and large-scale thin films becomes necessary for practical electronic and optical applications. Here, we report our recent progress in developing single-crystalline thin films with improved quality and their optical devices including Cd_3As_2-based heterojunctions and ultrafast optical switches. We find that a post-annealing process can significantly enhance the crystallinity of Cd_3As_2 in both intrinsic and Zn-doped thin films. With excellent characteristics of high mobility and linear band dispersion, Cd_3As_2 exhibits a good optical response in the visible-to-mid-infrared range due to an advantageous optical absorption, which is reminiscent of 3D graphene. It also behaves as an excellent saturable absorber in the mid-infrared regime. Through the delicate doping process in this material system, it may further open up the long-sought parameter space crucial for the development of compact and high-performance mid-infrared ultrafast sources.

Keywords: topological Dirac semimetals, thin films, photodetectors, ultra-fast optical switches

PACS: 75.47.–m, 75.70.Tj, 73.43.–f **DOI:** 10.1088/1674-1056/ab3a91

1. Introduction

In remembrance of the renowned Chinese physicist Professor Kun Huang, who made significant contributions to the development of solid-state physics, we start with a brief introduction of his pioneering achievement. Huang's research was mainly involved with many aspects of phonon physics in solids. He is widely known for his collaboration with Max Born in writing the classic monograph — Dynamical Theory of Crystal Lattices. His contributions include the concept of polaritons, Huang scattering of x-ray, the Huang–Rys factor used for describing electron–phonon interaction, and the Huang–Zhu model used for calculating electron–longitudinal phonon interaction in quantum wells and superlattices.[1–8] In recent years, Huang's research has been widely used to study various physical problems related to low-dimensional semiconductor materials and phonons, including transport phenomena, Raman scattering, phonon polaritons, and many other frontier problems.[9–11]

While the theoretical development of phonon dynamics has tremendously benefited the academia and semiconductor industries, the novel concept of topological matters was proposed and specific material systems were discovered in recent years. One representative example of topological systems is the topological insulator (TI), which features bulk states that have an energy bandgap and gapless surface states, allowing surface carriers to have zero effective mass.[12,13] Another intriguing example is topological Dirac semimetals (TDSs). They are a new kind of Dirac material that exhibits linear energy dispersion in the bulk and can be viewed as 3D graphene. It has been proposed that TDSs can be driven to other exotic phases like Weyl semimetals and topological insulators by breaking certain symmetries. One of the most exotic physical properties of these new materials is the chirality of electrons, where the spins of electrons are in parallel or antiparallel to the direction of their motion and thus develop the right-handed or left-handed chiral electrons (widely conceived as chiral anomaly). Theories also predict that topological Dirac semimetals can be driven into a quantum spin Hall insulator with a sizeable bandgap by reducing dimensionality. Driven by these exotic physical properties, extensive experiments on angle-resolved photoemission spectroscopy,[14–17] and scanning tunneling microscopy[18] were carried out to identify the 3D Dirac fermions in these materials.

The intriguing physics of these TDSs has motivated a surge of research activities towards the development of large-

*Project supported by the National Key Research and Development Program of China (Grant Nos. 2017YFA0303302 and 2018YFA0305601) and the National Natural Science Foundation of China (Grant Nos. 61322407, 11474058, 61674040, and 11874116).

†Corresponding author. E-mail: yshi@nju.edu.cn

© 2019 Chinese Physical Society and IOP Publishing Ltd

scale single-crystalline films for potential applications in electronics and optics. The Cd_3As_2 is considered to be an excellent 3D TDS due to its chemical stability in air, and it also possesses novel transport phenomena such as ultra-high mobility,[19] large magnetoresistance (MR),[20] nontrivial π Berry's phase of Dirac fermions,[21] and chiral anomaly induced negative MR.[22,23] Previously, Cd_3As_2 bulk materials, amorphous films,[24] nanowires,[25] and platelets[26] were prepared by various growth methods, and most of magneto-transport measurements so far have focused on Cd_3As_2 bulk materials. However, few efforts were devoted to thin films[27–29] and nanostructures,[25,30] which may exhibit surface phase-coherent transport and quantum size limit effect,[31–33] leading to Aharonov–Bohm oscillations[34] and quantum Hall insulator states.[35] Importantly, a theoretically-predicted TI phase and thickness-dependent quantum oscillations may also eventually emerge when the dimensionality of the system is reduced.[35,36] Therefore, it is highly desirable to fabricate superb crystallinity Cd_3As_2 thin films for the transport study, and to develop the possible optoelectronic applications by using the Cd_3As_2 thin film system. Here we present a brief review of our recent progress in making such ultra-high mobility Cd_3As_2 thin films via the post-annealing process and in making heterojunction photodetectors and ultrafast optical switches.[37–40]

2. Electrical transport study in intrinsic Cd_3As_2 thin films

A series of wafer-scale Cd_3As_2 thin films were grown via a molecular beam ppitaxy (MBE) system at a base pressure lower than 2×10^{-10} mbar (1 bar = 10^5 Pa). Single-polished sapphire and clean cleaved mica substrates were selected for electrical transport measurements. Before growing the Cd_3As_2 layer, the substrates were degassed at 400 °C for 30 min to remove gas molecules absorbed on the surface. Especially, a buffer layer of CdTe was deposited on the substrates in order to achieve a better crystalline match. The Cd_3As_2 thin film deposition was carried out on the top of the buffer layer with high-purity Cd_3As_2 (99.999%) from dual-filament and valve-cracker effusion cells. The growth process and film thickness awere *in situ* monitored by the reflection high-energy electron diffraction (RHEED).

3. Results

As displayed in Fig. 1(a), a standard six-probe Hall bar geometry is patterned on the Cd_3As_2 thin film with a channel size of 1.5 mm×1 mm. Low-temperature electrical transport measurements are carried out for samples with filme different

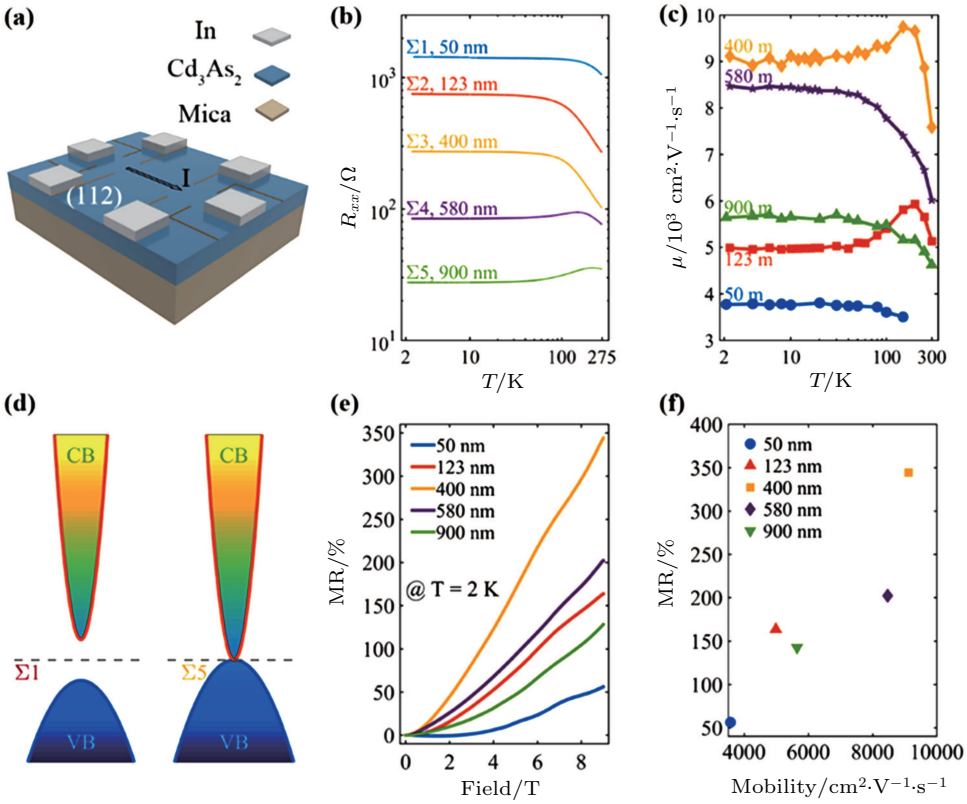


Fig. 1. (a) Schematic diagram of standard six-probe Hall bar fabricated on Cd_3As_2 thin films with mica substrate, used for transport measurements in the PPMS system. Crystal orientation is (112), which is perpendicular to the magnetic field (up to 9 T). (b) Zero-field temperature-dependent longitudinal resistance R_{xx} curves for five Cd_3As_2 thin films with different thicknesses ranging from 50 nm to 900 nm; R_{xx} drops with sample thickness reducing, indicating a thickness-induced insulator-to-metal transition. (c) Variations of carrier mobility μ with temperature. Carrier mobility is about 3750 $cm^2 \cdot V^{-1} \cdot s^{-1}$–9750 $cm^2 \cdot V^{-1} \cdot s^{-1}$ at 2 K. (d) Sketch of band structure with band gap opening for Cd_3As_2 thin films. (e) MR ratio at 2 K, showing non-saturation behavior and the largest ratio reaching 343.5%. (f) Nearly linear relationship between MR and electron mobility, which drops from 343.5% to 58.8%. Figure 1 is adapted from Ref. [38].

thickness in a physical properties measuring system (PPMS, up to 9 T). The zero-field resistance–temperature (R–T) curves of longitudinal magnetoresistance R_{xx} of the Cd_3As_2 thin films with different thicknesses are shown in Fig. 1(b) (Σ1–Σ5). Meanwhile, the transverse resistance (R_{xy}) *versus* magnetic field B is measured at $T = 2$ K, where the negative slope of R_{xy} shows that electrons are the dominant charge carriers in intrinsic Cd_3As_2 thin films. As shown in Fig. 1(c), derived from the R_{xy}–B linear parts, the typical temperature-dependence of Hall mobility (μ) is in a range of 3.8×10^3 cm^2·V^{-1}·s^{-1}–9.1×10^3 cm^2·V^{-1}·s^{-1} at 2 K. The mobility significantly increases as the temperature T drops, which can be attributed to the alleviated electron–phonon scattering at low temperatures. Besides, the sheet carrier density (n_s) at 2 K changes from 3.4×10^{12} cm^{-2} to 24×10^{12} cm^{-2}, and the corresponding carrier concentration (n_{3D}) is determined to be 1×10^{17} cm^{-3}–8×10^{17} cm^{-3}. Figure 1(d) shows a band schematic structure for a typical Cd_3As_2 thin film. When the dimensionality is reduced, a gap is expected to open. The Fermi levels marked in the diagrams are calculated from Shubnikov–de Haas (SdH) quantum oscillations, which will be discussed below. Comparing with the R_{xx}–T curves mentioned above, the relative position between Fermi levels and band edges is almost consistent with each other. Moreover, figure 1(e) exhibits that a large positive magnetoresistance (MR) at 2 K in a series of Cd_3As_2 films shows a parabolic behavior at low fields and quasi-linear property at high fields ($B \geq 5$ T). It does not show a saturated tendency when the magnetic field increases, and the maximum MR ratio is close to 343.5% at $B = 9$ T. Especially, related to the electron mobility, the corresponding MR ratio at 9 T drops from 343.5% to 58.8%. As shown in Fig. 1(f), there exists an almost linear relationship between the MR ratio and mobility, which is consistent with the previous study.[41] Due to the Dirac band structure and the high mobility in Cd_3As_2 thin films, there are strong SdH quantum oscillations in R_{xx} for most of our samples at 2 K as shown in Fig. 1(e).

3.1. Post-annealing effect on intrinsic and Zn-doped Cd_3As_2 thin films

In order to further enhance the crystalline quality, the as-grown films were annealed at elevated temperatures after depositing a 120-nm-thick Al_2O_3 capping layer on the top. It can protect the underlying thin films from being oxidized in the annealing process. Figure 2(a) illustrates the structure of the multi-layered film. Figure 2(b) shows the XRD spectra which are enlarged to highlight the change of the Cd_3As_2 (224) peaks marked by the grey dashed line. The broader peak at the left of the (224) peak comes from CdTe (111). It is evident that (224) peaks become sharper as the annealing temperature increases. In Fig. 2(c) summarized is the variation of the full width at half maximum (FWHM), which indicates that the Cd_3As_2 film undergoes recrystallization after annealing procedure that effectively reduces the FWHM.

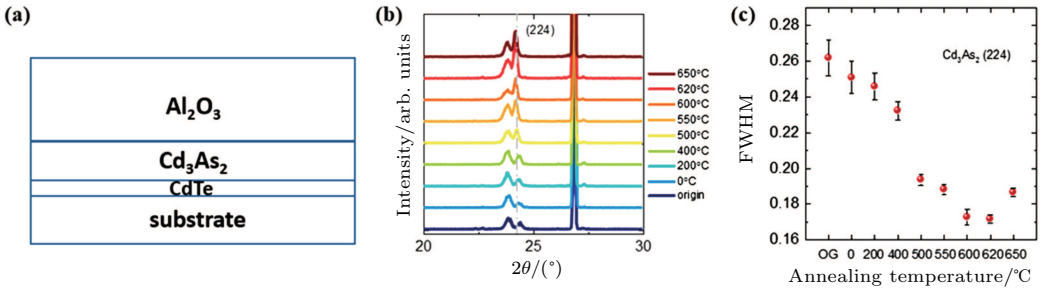


Fig. 2. (a) Schematic illustration of capping and annealing film structure, (b) XRD patterns at different annealing temperatures, (c) value of FWHM varying with annealing temperature. Experimental data denoted as 0 °C in panels (b) and (c) represent the results for samples before annealing but after ALD process; and origin and OG in panels (b) and (c), respectively, represent samples before the ALD process.

The post-annealing process brings about a significant enhancement of quantum oscillations. Figures 3(a) and 3(b) show the normalized resistance changes with temperature at different annealing temperatures. Below 650 °C, the samples show a metallic behavior with a small upturn at low temperatures. In a temperature range of 0 °C–550 °C, the residue resistance ratio (RRR) decreases with the increase of annealing temperature. Once the temperature reaches 650 °C, the film shows a semiconducting behavior.

The small upturn in the R–T curves at low temperatures could have two origins. One is electron–electron interaction, and the other is weak localization. Both of the two mechanisms will lead to a very similar upturn feature in the R–T curve, *i.e.*, the R–T curve will be linear in the logarithmic scale at low temperatures. We examine the linear behaviors of several samples and suggest that the contribution from localization is the main contribution to the metallic-insulating transition. We then study the MRs of these samples at 2 K. As shown in Figs. 3(c) and 3(d), the sample without and with annealing (at 200 °C) shows a negative MR accompanied by SdH oscillations. By further increasing the annealing temperature, the negative MR decreases but the oscillation amplitude is unchanged. When the annealing temperature exceeds 400 °C, the amplitude of oscillation is dramatically enlarged.

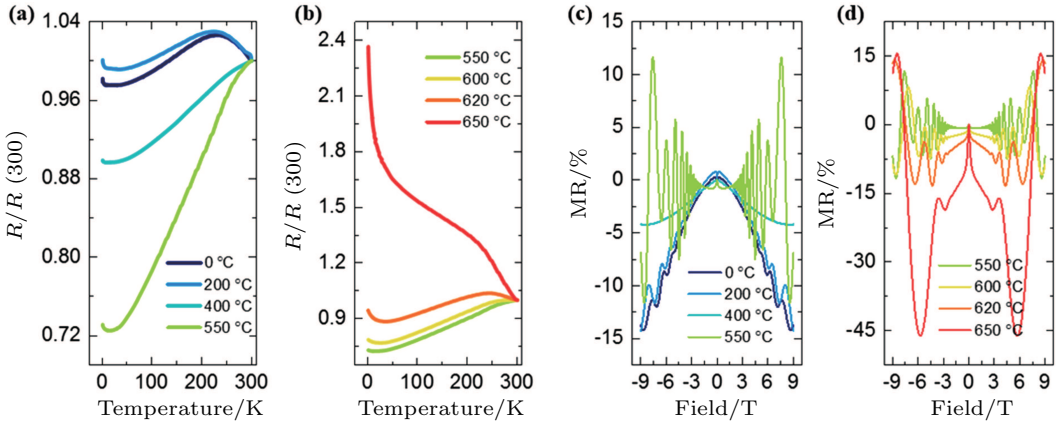


Fig. 3. (a) and (b) *R*–*T* curves with different annealing temperatures, showing that RRR decreases with annealing temperature increasing when $T < 550$ °C, tendency is opposite above 550 °C, and a semiconducting property occurs at higher annealing temperatures; (c) and (d) curves of oscillation amplitudes versus field, indicating that amplitude increases with annealing temperature rising.

Further, Zn is doped into Cd_3As_2 to reduce the Fermi level. The size of Fermi surface can be extracted from the SdH oscillations. With the Zn concentration increasing, the oscillation frequency (S_F) decreases and the Fermi level decreases as summarized in Table 1. For the samples with low Zn concentration, it is easier to reach a quantum limit at high magnetic fields.

Table 1. Fermi level decreasing with Zn concentration increasing.

Sample number	1	2	3
x for $(Zn_xCd_{1-x})_3As_2$	0	10%	8.5%
S_F/T	23.4	9.8	10.8

In short, the rapid annealing process can enhance the crystal quality by reducing defects via developing a recrystallization process. After annealing, the mobility of thin films rises, while the SdH oscillations become strikingly stronger.

3.2. Cd_3As_2 heterojunction photodetectors

Based on the high-quality Cd_3As_2 thin films, a Cd_3As_2/pentacene heterojunction photodetector is fabricated as shown in Fig. 4(a). The diagram of Cd_3As_2/pentacene heterojunction is described in Fig. 4(b). A positively-charged empty state exists in the depletion region in n-type Cd_3As_2, when electrons move from the n-type Cd_3As_2 into the lower energy states of the p-type pentacene. The band is bent up near the heterojunction to form a built-in field. Pentacene, as a kind of organic matter, is chosen as the p-type material in heterojunction photodetector. The organics is accessible and low-cost so that they are hopeful to be applied to large-scale devices. Besides, the dark current of organics is low, which is important for photodetectors.

For heterojunction-based photodetectors, the *I*–*V* curve shows a rectification characterisitics of the photodetector with or without illumination, and we select the appropriate bias voltage (V_{bias}) which is exhibited in Fig. 5(a). We chose 0.5 mV to be the main test V_{bias} according to the I_{ill}/I_{dark} ratio. The photocurrent curves of the Cd_3As_2/pentacene heterojunction are measured under different wavelengths 450 nm–1550 nm, with a laser power of 10 mW while 2800 nm and 10600 nm whose laser powers are nearly 5.8 mW and 50 mW. Figures 5(b) and 5(c) show the photocurrents of Cd_3As_2/pentacene heterojunction photodetectors without and with the bias voltage, respectively. Obviously, the photocurrents with V_{bias} are higher than those without V_{bias}. The wide-waveband photoelectric response is associated with the Cd_3As_2/pentacene heterojunction absorption. Figure 5(d) indicates that the photocurrent increases almost linearly with V_{bias} increasing, which means that the device is stable and consistent. The amplitude of the light current increases with the V_{bias} increasing. The above results manifest good periodicity and switching characteristics of the devices.

As shown in Fig. 5(e), the responsivity R_i is calculated with a bias voltage of 500 mV, for both Cd_3As_2/pentacene heterojunction photodetector and Cd_3As_2 thin film photodetector. The R_i of Cd_3As_2 thin film photodetector maximizes at 520 nm (12.5 mA/W), indicating a good current response. Compared with the Cd_3As_2 thin film photodetector, the Cd_3As_2/pentacene heterojunction displays an obvious advantage in the current response at every frequency. The largest R_i, *i.e.*, 36.15 mA/W appears at 650 nm. Besides, the R_i of pentacene has a maximum value of 8.6 mA/W at 650 nm. Furthermore, the external quantum efficiency (EQE) can describe the efficiency of light energy utilization. Figure 5(f) shows the dependence of EQE on wavelength of the Cd_3As_2/pentacene structure, indicating that the largest EQE is 7.29% at 650 nm. The high infrared response highlights the high performance of Cd_3As_2/pentacene heterojunction photodetector. For instance, the photodetector has the outstanding responsivity varying from 17.03 mA/W to 1.55 mA/W at different wavelengths, which is usually rare in graphene-based photodetectors. Because the communication band is located in a wavelength range between 980 nm and 1550 nm,[41,42] these photodetectors can be hopefully used in information communications.

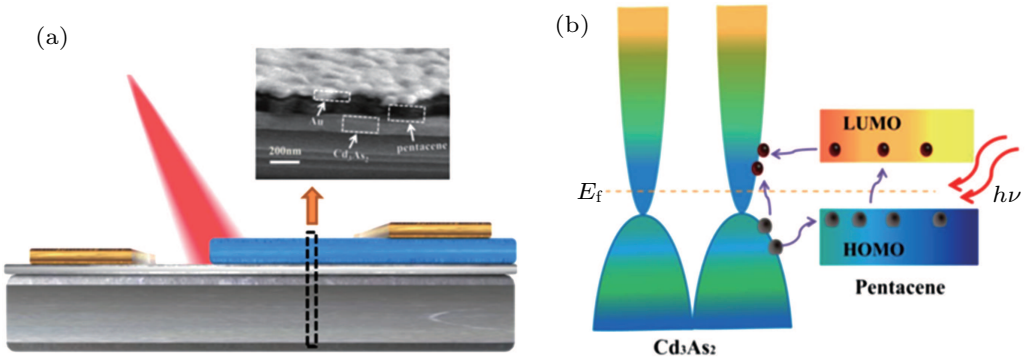


Fig. 4. (a) Schematic diagram of photocurrent measurement of Cd_3As_2 /pentacene heterojunction and transmission electron microscopy (TEM) diagram for the cross-section view. (b) Energy-band diagrams of ideal Cd_3As_2/pentacene heterojunction, where LUMO means the lowest unoccupied molecular orbital and HOMO means the highest occupied molecular orbital. This figure is partially adapted from Ref. [39], ACS Publications Group.

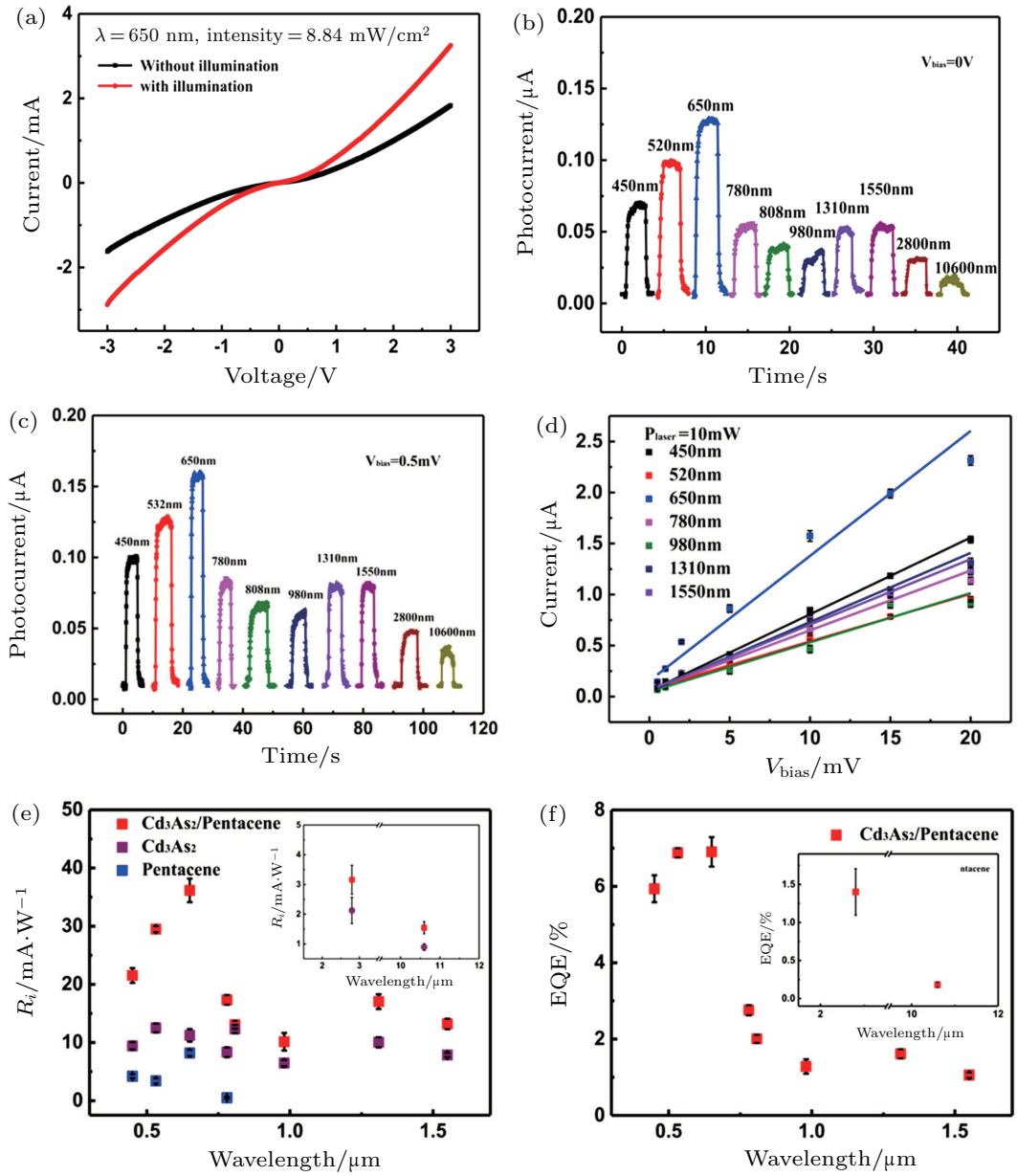


Fig. 5. (a) *I–V* curves of the Cd_3As_2 thin film/pentacene heterojunction photodetector with and without illumination at the wavelength of 650 nm. (b) and (c) Photocurrent curves of Cd_3As_2/pentacene heterojunction measured under different wavelengths without and with bias voltage, respectively. (d) Photocurrent curves with bias voltage at wavelengths of 450, 520, 650, 780, 980, 1310, and 1550 nm. (e) Comparison between responsivity (R_i) of Cd_3As_2 thin films/pentacene heterojunction photodetector and Cd_3As_2 thin film photodetector. (f) Wavelength-dependent EQE of Cd_3As_2/pentacene heterojunction photodetectors. This figure is adapted from Ref. [39], ACS Publications Group.

Compared with the pure Cd_3As_2 photodetector, the Cd_3As_2/pentacene photodetectors achieve an obvious improvement of R_i. The pentacene layer plays important roles in both the visible band and the infrared band. It has a good absorption in the visible spectrum, which means that it can absorb the light and then produce charges when the light is incident in the junction area of pentacene and Cd_3As_2. Thus, the R_i of the Cd_3As_2/pentacene heterostructure detector is much higher than that of the pure Cd_3As_2 thin film detector in the visible band. Since pentacene has proved to have a single peak exciton fission effect at about 660 nm, more conductive charges are generated when the light irradiates, which causes R_i to reach a maximum value at 650 nm. As a result, the R_i value of the Cd_3As_2/pentacene detector is also higher than that of the pure Cd_3As_2 thin film detector in the infrared band.

3.3. Cd_3As_2 mid-infrared optical switches

Since the early 1990 s, semiconductor saturable absorber mirrors (SESAMs) have been an important approach in the near-infrared field. Flexibility and preciseness make SESAMs one of the most important saturating absorber technologies, and it can be adapted into various laser formats, such as fibre, solid-state or semiconductor chip lasers.[43–45] By detecting the mid-infrared optical response of the bulk Dirac fermions, it is found that MBE-grown Cd_3As_2 thin films can act as an excellent ultra-fast (< 10 ps) optical switch in the mid-infrared, with a working range covering at least 3 μm–6 μm.

We carry out pump-probe measurements on the intrinsic and Cr-doped Cd_3As_2 thin films. The non-degenerate transient transmission spectroscopy reveals photo-bleaching characteristics caused by Pauli blockage, according to which we show that Cd_3As_2 has a saturated absorption characteristics over the entire spectral range (Fig. 6(a)). We summarize all the fitted time constants in Fig. 6(b), which clearly shows that MBE-grown Cd_3As_2 films exhibit ultrafast saturated absorption at mid-infrared wavelengths ranging from 3 μm to 6 μm. Figure 6(c) displays the power-dependent transmittance of Cd_3As_2 thin film. Here, the transmittance is determined from $T(l) = 1 - \Delta T \cdot \exp[-I/I_{\text{sat}}] - T_{\text{ns}}$, where I, I_{sat}, ΔT, and T_{ns} respectively denote input intensity, saturation intensity, modulation depth, and non-saturable absorbance. A simple saturation model[46] can fit the measurement data. As shown in Fig. 6(c), this system can yield a modulation depth of $\sim 4.4\%$. In addition, the powerful parametric customization of the Cd_3As_2 allows the on-demand access to different pulse states in 3-μm fiber laser, indicating the potential for a significant increase in the performance level of mid-infrared pulsed laser. Compared with some lasers made of low-dimensional materials such as graphene and black phosphorus,[47,48] the laser made of Cd_3As_2 film possesses advantages, such as scaling to longer mid-infrared wavelength as well as flexibility in customizing the relaxation time.

To illustrate the benefits of expanding the parameter space through a delicate Cr doping, we demonstrate on-demand access to different pulse states for domestic 3-μm fluoride fiber lasers using Cd_3As_2 films with different relaxation times. A fiber laser test bench is chosen, and the demonstration can also be carried out on other mid-infrared lasers, such as an extra-cavity semiconductor laser. The pulsed laser setup is shown in Fig. 7(a). Firstly, we use an un-doped Cd_3As_2 film with a relatively long time constant (~ 7 ps at a wavelength of ~ 3 μm). As can be seen from Fig. 7(b), it appears that the continuous wave (CW) emission becomes the Q-switched mode-lock envelope when the pump power reaches 58 mW.

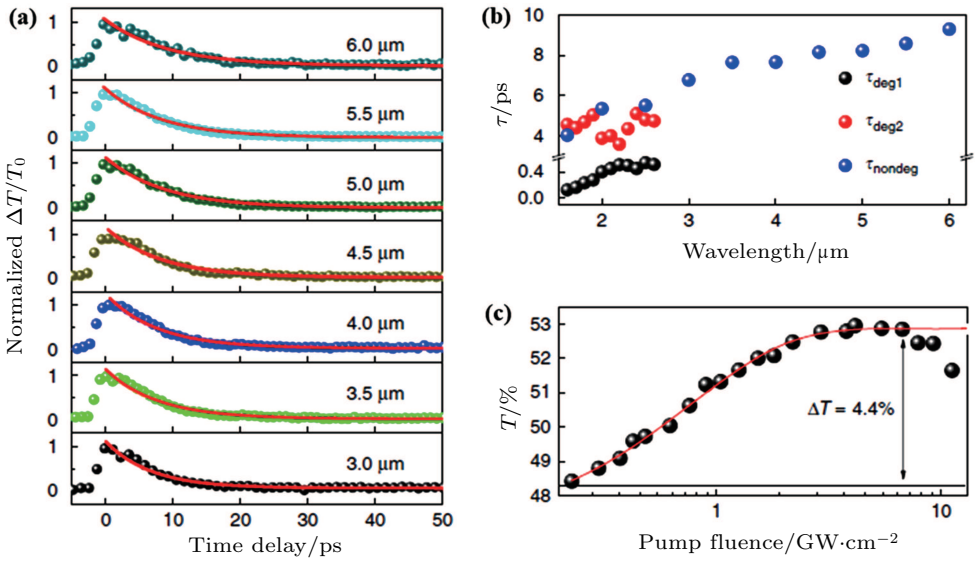


Fig. 6. (a) Non-degraded ultrafast pump-probe results at probe wavelengths between 3 μm and 6 μm, and solid red line corresponding to single exponential fit of τ_{nondeg}. (b) Fitted plots of relaxation time constant τ *versus* probing wavelength for both degenerate (black and red points) and non-degenerate (blue points) measurements. (c) Nonlinear absorption at wavelength 3 μm (black points) and fitting with simple saturation model (red line). This figure is adapted from Ref. [40], Nature Publishing Group.

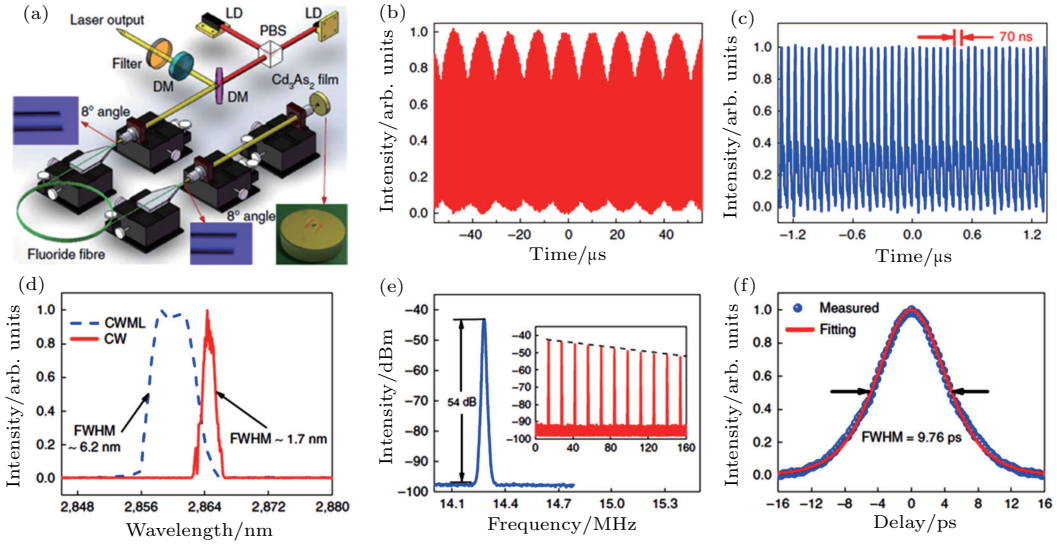


Fig. 7. (a) Schematic diagram of fibre laser setup, where LD, PBS, and DM are diode laser, polarized beam splitter, and dichroic mirror, respectively. (b) *Q*-switched mode-locked pulses at pump power 57.6 mW. (c) CW mode-locked (CWML) pulses at pump power 286.9 mW. No discernable envelope modulation indicates stable operation. (d) Output optical spectrum. Because reduction in intracavity loss results in a lower initial Stark manifold of the $^5I_6$ level, center wavelength of continuous wave operation is red-shifted to 2864.3 nm. At the same time, since required spectral Fourier component is small, the full width at a half maximum reduces to 1.7 nm. (e) Radio frequency (RF) spectra have scan range 0.8 MHz and resolution bandwidth 10 kHz, with repetition rate and signal-to-noise ratios being 14.28 MHz and 54 dB, respectively. Inset shows RF spectra with broader scans ranging from 0 to 160 MHz. (f) Autocorrelation curve measured with intensity autocorrelator. Blue points are experimental results, and red line refers to the fitting results from sech function. This figure is adapted from Ref. [40], Nature Publishing Group.

As the pump power further increases, the duration and period of the *Q*-switched envelope both shorten as expected. As displayed in Fig. 7(c), the *Q*-switched mode-locking state quickly changes into CW mode-locking when the pump power becomes 80 mW, and the pump power can be maintained up to 290 mW. The pulse period of 70 ns is consistent with the calculated cavity round trip time. Figure 7(d) displays the optical spectrum of the mode-locked pulses. The center wavelength can reach 2860 nm and the FWHM can be 6.2 nm. Moreover, as shown in Fig. 7(e), the radio-frequency spectra of the pulses are also measured to determine a robust and stable mode-locking operation. Figure 7(f) shows that the pulse duration is measured by using a home-made mid-infrared autocorrelator and the pulse width is estimated at 6.3 ps. It is clear that un-doped sample could achieve stable mode locking. The Cr-doped Cd_3As_2 film with a shorter relaxation time is then introduced into the cavity in turn. It is found that as the relaxation time of Cd_3As_2 is shortened, the threshold for CW mode-locking increases because the higher intensity is now required to saturate the conduction band.

4. Conclusions and perspectives

Cd_3As_2, as a topological Dirac semimetal in three-dimensionality, has shown a quantum Hall effect (QHE) in both nanostructures and thin films.[49–51] Particularly, our group has reported the 3D Weyl-orbit-based QHE in Cd_3As_2 nanoplates.[52] Hence, with the mobility increasing, it is hopeful to achieve high-quality thin films in the quantum Hall regime. In this regard, the Zn doping can validly reduce the Fermi level, which makes the films easier to reach the quantum limit. Therefore, the electron–electron interactions can be significantly enhanced as demonstrated by several recent experiments on the phase transitions of several topological semimetals.[53,54] Thus, it is quite exciting to continue improving the crystalline quantity of Cd_3As_2 films as well as the effective Zn doping, to envisage the exotic 3D quantum behavior in topological semimetal systems.

While the fundamental research on new topological physics and the various emergent phenomena continue to be conducted, we attempt the potential utilization of topological properties in practice. The Cd_3As_2 has proved to have an extraordinary optical response. Since the Cd_3As_2/pentacene heterojunction device can raise the responsivity and external quantum efficiency in a broad range from visible light to far-infrared light, it is feasible to use the heterostructures of Cd_3As_2 and organic molecules to construct the photodetectors. Along this route, we expect to realize the devices with higher responsivity and external quantum efficiency with different organic molecules, and make the responsive range much broader (towards THz).[55] Considering the excellent broadband responsiveness of these Cd_3As_2/organic thin film photodetectors, our work provides a new approach to applying the 3D TDSs to optoelectronic devices.

Furthermore, the attempt of using Cd_3As_2 as a saturable absorber in the field of pulsed lasers seems to be quite successful. The key characteristics including comprehensive scalability, broadband operation, and flexible parameter control effectively establish Cd_3As_2 as a highly adaptable near-infrared SESAM.[56–58] In development, we anticipate the proposed

electrically contacted saturable absorber device. It can be further extended to active photonic devices operating in the near- to far-infrared range, including optical modulators and tunable light-emitting devices.

In short, our research on high-quality Cd_3As_2 thin films paves the way for applying the 3D TDSs to photodetectors and presents a feasible approach to preparing the large-scale array photodetectors. Meanwhile, our work represents a step forward in the development of compact mid-infrared ultrafast sources for advanced sensing, communication, spectroscopy, and medical diagnostics using topological Dirac semimetal materials.

References

[1] Peisl H, Spalt H and Waidelich W 1967 *Phys. Stat. Solidi* **23** K75
[2] Huang K 1951 *Nature* **167** 779
[3] Henry C H and Hopfield J J 1965 *Phys. Rev. Lett.* **15** 964
[4] Huang K and Rhys A 1950 *Proc. Roy. Soc. (London)* **A204** 406
[5] Born M and Huang K 1954 *Theory of Crystal Lattice Dynamics* (Oxford: Oxford University Press)
[6] Huang K and Zhu B F 1988 *Phys. Rev. B* **38** 2183
[7] Huang K and Zhu B F 1988 *Phys. Rev. B* **38** 13377
[8] Pioneer of Phonon Physics: Kun Huang, https://pyyuwp.wordpress.com/
[9] Tsen K T, Wald K R, Ruf T, Yu P Y and Morkoç H 1991 *Phys. Rev. Lett.* **67** 2557
[10] Heitz R, Mukhametzhanov I, Stier O, Madhukar A and Bimberg D 1999 *Phys. Rev. Lett.* **83** 4654
[11] Shields A J, Chamberlain M P, Cardona M and Eberl K 1995 *Phys. Rev. B* **51** 17728
[12] Hasan M Z and Kane C L 2010 *Rev. Mod. Phys.* **82** 3045
[13] Qi X L and Zhang S C 2011 *Rev. Mod. Phys.* **83** 1057
[14] Borisenko S, Gibson Q, Evtushinsky D, Zabolotnyy V, Büchner B and Cava R J 2014 *Phys. Rev. Lett.* **113** 027603
[15] Neupane M, Xu S Y, Sankar R, Alidoust N, Bian G, Liu C, Belopolski I, Chang T R, Jeng H T, Lin H, Bansil A, Chou F and Hasan M Z 2014 *Nat. Commun.* **5** 3786
[16] Liu Z K, Jiang J, Zhou B, Wang Z J, Zhang Y, Weng H M, Prabhakaran D, Mo S K, Peng H, Dudin P, Kim T, Hoesch M, Fang Z, Dai X, Shen Z X, Feng D L, Hussain Z and Chen Y L 2014 *Nat. Mater.* **13** 677
[17] Yi H, Wang Z, Chen C, Shi Y, Feng Y, Liang A, Xie Z, He S, He J, Peng Y, Liu X, Liu Y, Zhao L, Liu G, Dong X, Zhang J, Nakatake M, Arita M, Shimada K, Namatame H, Taniguchi M, Xu Z, Chen C, Dai X, Fang Z and Zhou X J 2015 *Sci. Rep.* **4** 6106
[18] Jeon S, Zhou B B, Gyenis A, Feldman B E, Kimchi I, Potter A C, Gibson Q D, Cava R J, Vishwanath A and Yazdani A 2014 *Nat. Mater.* **13** 851
[19] Liang T, Gibson Q, Ali M N, Liu M, Cava R J and Ong N P 2015 *Nat. Mater.* **14** 280
[20] Feng J, Pang Y, Wu D, Wang Z, Weng H, Li J, Dai X, Fang Z, Shi Y and Lu L 2015 *Phys. Rev. B* **92** 081306
[21] He L P, Hong X C, Dong J K, Pan J, Zhang Z, Zhang J and Li S Y 2014 *Phys. Rev. Lett.* **113** 246402
[22] Li C Z, Wang L X, Liu H, Wang J, Liao Z M and Yu D P 2015 *Nat. Commun.* **6** 10137
[23] Li H, He H, Lu H Z, Zhang H, Liu H, Ma R, Fan Z, Shen S Q and Wang J 2016 *Nat. Commun.* **7** 10301
[24] Dubowski J J and Williams D F 1984 *Appl. Phys. Lett.* **44** 339
[25] Schönherr P and Hesjedal T 2015 *Appl. Phys. Lett.* **106** 013115
[26] Lovett D R 1972 *J. Mater. Sci.* **7** 388
[27] Din M and Gould R D 2006 *Appl. Surf. Sci.* **252** 5508
[28] Liu Y, Zhang C, Yuan X, Lei T, Wang C, Di D, Narayan A, He L, Picozzi S, Sanvito S, Che R and Xiu F 2015 *NPG Asia Mater.* **7** e221
[29] Zhao B, Cheng P, Pan H, Zhang S, Wang B, Wang G, Xiu F and Song F 2016 *Sci. Rep.* **6** 22377
[30] Zhang E, Liu Y, Wang W, Zhang C, Zhou P, Chen Z G, Zou J and Xiu F 2015 *ACS Nano* **9** 8843
[31] Portal J C, Moaty M A, Żdanowicz W and Żdanowicz L 1981 *Thin Solid Films* **76** 391
[32] Żdanowicz W, Żdanowicz L, Portal J C and Askenazy S 1979 *Thin Solid Films* **61** 41
[33] Żdanowicz L, Żdanowicz W and Pocztowski G 1975 *Thin Solid Films* **28** 345
[34] Wang L X, Li C Z, Yu D P and Liao Z M 2016 *Nat. Commun.* **7** 10769
[35] Wang Z, Weng H, Wu Q, Dai X and Fang Z 2013 *Phys. Rev. B* **88** 125427
[36] Potter A C, Kimchi I and Vishwanath A 2014 *Nat. Commun.* **5** 5161
[37] Zhang C, Lu H Z, Shen S Q, Chen Y P and Xiu F X 2018 *Sci. Bull.* **63** 580
[38] Cheng P H, Zhang C, Liu Y W, Yuan X, Song F Q, Sun Q Q, Zhou P, Zhang D W and Xiu F X 2016 *New. J. Phys.* **18** 083003
[39] Yang M, Wang J, Han J Y, Ling J W, Ji C H, Kong X, Liu X C, Huang Z H, Gou J, Liu Z J, Xiu F X and Jiang Y D 2018 *ACS Photon.* **5** 3438
[40] Zhu C H, Wang F Q, Meng Y F, Yuan X, Xiu F X, Luo H Y, Wang Y Z, Li J F, Lv X J, He L, Xu Y B, Liu J F, Zhang C, Shi Y, Zhang R and Zhu S N 2017 *Nat. Commun.* **8** 14111
[41] Fernández-MerinoL M J, Guardia L, Paredes J I, Villar-Rodil S, Solís-Fernández P, Martínez-Alonso A and Tascón J M D 2010 *J. Phys. Chem. C* **114** 6426
[42] Wang Q S, Li C Z, Ge S F, Li J G, Lu W, Lai J, Liu X F, Ma J C, Yu D P, Liao Z M and Sun D 2017 *Nano Lett.* **17** 834
[43] Keller U 2003 *Nature* **424** 831
[44] Keller U, Miller D A B, Boyd G D, Chiu T H, Ferguson J F and Asom M T 1992 *Opt. Lett.* **17** 505
[45] Keller U, Weingarten K J, Karter F X, Kopf D, Braun B, Jung I D, Fluck R, Honniger C, Matuschek N and J Aus der Au 1996 *IEEE J. Sel. Top. Quantum Electron.* **2** 435
[46] Chen Y, Zhao C J, Chen S Q, Du J, Tang P H, Jiang G B, Zhang H, Wen S C and Tang D Y 2014 *IEEE J. Sel. Top. Quantum Electron.* **20** 0900508
[47] Qin Z P, Xie G Q, Zhao C J, Wen S C, Yuan P and Qian L J 2016 *Opt. Lett.* **41** 56
[48] Zhang Y Z, Liu T, Meng B, Li X H, Liang G Z, Hu X N, Hu X N and Wang Q J 2013 *Nat. Commun.* **4** 1811
[49] Zhang C, Narayan A, Lu S H, Zhang J L, Zhang H Q, Ni Z L, Yuan X, Liu Y W, Park J H, Zhang E, Wang W Y, Liu S S, Cheng L, Pi L, Sheng Z G, Sanvito S and Xiu F X 2017 *Nat. Commun.* **8** 1272
[50] Uchida M, Nakazawa Y, Nishihaya S, Akiba K, Kriener M, Kozuka Y, Miyake A, Taguchi Y, Tokunaga M, Nagaosa N, Tokura Y and Kawasaki M 2017 *Nat. Commun.* **8** 2274
[51] Timo Schumann, Luca Galletti, Kealhofer A, Honggyu Kim, Manik Goyal and Susanne Stemmer 2018 *Phys. Rev. Lett.* **120** 016801
[52] Zhang C, Zhang Y, Yuan X, Lu S H, Zhang J L, Narayan A, Liu Y W, Zhang H Q, Ni Z L, Liu R, Choi E S, Suslov A, Sanvito S, Pi L, Lu H Z, Potter A C and Xiu F X 2019 *Nature* **565** 331
[53] Liu Y W, Yuan X, Zhang C, Jin Z, Narayan A, Luo C, Chen Z G, Yang L, Zou J, Wu X, Sanvito S, Xia Z C, Li L, Wang Z and Xiu F X 2016 *Nat. Commun.* **7** 12516
[54] Zhang C L, Tong B B, Yuan Z J, Lin Z Q, Wang J F, Zhang J L, Xi C Y, Wang Z, Jia S and Zhang C 2016 *Phys. Rev. B* **94** 205120
[55] Yang M, Wang J, Yang Y K, Zhang Q, Ji C H, Wu G R, Su Y J, Gou Jun, Wu Z M, Yuan K J, Xiu F X and Jiang Y D 2019 *J. Phys. Chem. Lett.* **10** 3914
[56] Zhu C H, Yuan X, Xiu F X, Zhang C, Xu Y B, Zhang R, Shi Y and Wang F Q 2017 *Appl. Phys. Lett.* **111** 091101
[57] Meng Y F, Zhu C H, Li Y, Yuan X, Xiu F X, Shi Y, Xu Y B and Wang F Q 2018 *Opt. Lett.* **43** 1503
[58] Sun Y, Meng Y F, Jiang H Z, Qin S C, Yang Y K, Xiu F X, Shi Y, Zhu S N and Wang F Q 2019 *Opt. Lett.* **44** 582